

Correlation Between Optical and X-ray Break Frequencies in Power Spectra of Active Galactic Nuclei

HEECHAN YUK,¹ XINYU DAI,¹ T. JAYASINGHE,^{2,*} PATRICK J. VALLELY,^{3,†}
CHRISTOPHER S. KOCHANEK,^{3,4} BENJAMIN J. SHAPPEE,⁵ AND K. Z. STANEK^{3,4}

¹*Homer L. Dodge Department of Physics and Astronomy, University of Oklahoma, Norman, OK 73019, USA*

²*Department of Astronomy, University of California Berkeley, Berkeley CA 94720, USA*

³*Department of Astronomy, The Ohio State University, 140 West 18th Avenue, Columbus, OH 43210, USA*

⁴*Center for Cosmology and AstroParticle Physics, The Ohio State University, 191 W. Woodruff Ave., Columbus, OH 43210, USA*

⁵*Institute for Astronomy, University of Hawai'i at Manoa, 2680 Woodlawn Dr., Honolulu, HI 96822, USA*

ABSTRACT

We analyze the optical power spectral density (PSD) for 22 active galactic nuclei (AGN) with measured X-ray PSDs using light curves from the All-Sky Automated Survey for SuperNovae (ASAS-SN) and the Transiting Exoplanet Survey Satellite (TESS). The joint optical PSD is measured over up to six orders of magnitude in frequency space from timescales of minutes to a decade. We fit either a damped random walk (DRW) or a broken power law model to constrain the PSD model and break frequency. For the broken power-law fits to the joint PSDs, we find a high-frequency timescale which is proportional to both the X-ray timescales and the black hole masses, but the optical timescale is 2.7 dex longer. Assuming the optical and X-ray breaks are related by a physical process, such as reprocessing of X-ray emission, the break frequency difference interpreted as a light crossing time is consistent with the expected size difference between the optical and X-ray emission regions. On timescales of months to a decade, we also measured a correlation between the low-frequency optical break timescales and the X-ray break timescales, but with a much shallower slope. The DRW model provides acceptable fits and we generally confirm previously reported correlations between the DRW timescales and the black hole mass.

1. INTRODUCTION

Variability is a ubiquitous characteristic of active galactic nuclei (AGNs), and is observed at all wavelengths (e.g., Mushotzky et al. 1993; Vanden Berk et al. 2004) and on all timescales (e.g., Grandi et al. 1992; Markowitz et al. 2003). The mechanism driving the variability is still debated. A number of theories have been suggested, such as accretion disk instabilities (e.g., Kawaguchi et al. 1998;

hyuk@ou.edu

xdai@ou.edu

* NASA Hubble Fellow

† NSF Graduate Research Fellow

Trèvese & Vagnetti 2002), global inhomogeneities from infall or thermal processes (e.g., Lightman & Eardley 1974; Shakura & Sunyaev 1976; Kelly et al. 2009), local disk communication processes on sound crossing or Alfvén timescales (Dexter & Agol 2011), magnetorotational instabilities (e.g., Balbus & Hawley 1991; Reynolds & Miller 2009), and reprocessing between the disk and the corona on light crossing timescales (e.g., Haardt & Maraschi 1991; McHardy et al. 2018).

Though its origin is uncertain, AGN variability provides clues about the physical properties of the central engine. The variability at different wavelengths is known to arise from different regions of the AGN, and the variability time lags in different wavelengths can be used for reverberation mapping to measure the physical size of the AGN structure and the mass of the central supermassive black hole (SMBH) (e.g., Wandel et al. 1999; Kaspi et al. 2000; Peterson et al. 2005). Different classes of AGN also show different variability features (e.g., Ptak et al. 1998), and by studying these differences, we can learn specific details about each class. As a behavior common to all AGN, variability can also be used to find AGN (e.g., Butler & Bloom 2011; MacLeod et al. 2011; Ruan et al. 2012; Treiber et al. 2022; Yuk et al. 2022).

The stochastic variability of AGN can be characterized by its power spectral density (PSD). The PSDs are characterized by red noise, where the power increases for lower frequencies and then saturates below some frequency (e.g., Uttley et al. 2002). For optical variability this is commonly modeled as a damped random walk (DRW) (e.g., Kelly et al. 2009; Kozłowski 2016). In these models, the DRW break frequency, the frequency where the PSD starts to flatten, is correlated with the mass of the SMBH powering the AGN (e.g., Kelly et al. 2009; MacLeod et al. 2010; Burke et al. 2021).

The X-ray variability of AGN is observed down to very short timescales ($< \text{day}$) (e.g., Grandi et al. 1992; Uttley et al. 2002), with many PSD and break frequency studies (e.g., Uttley et al. 2002; McHardy et al. 2004; González-Martín & Vaughan 2012; González-Martín 2018; Smith et al. 2018). With the recent advent of high-cadence optical data, we can now probe the optical PSD on these short timescales (e.g., Smith et al. 2018). For this study, we combine the long-term, low-cadence, ground-based data from the All-Sky Automated Survey for SuperNovae (ASAS-SN; Shappee et al. 2014a; Kochanek et al. 2017) and the short-term, high-cadence, space-based data from the Transiting Exoplanet Survey Satellite (TESS; Ricker et al. 2015). We construct a PSD separately for each data set and then merge them to identify the break frequencies. This allows the first systematic comparison of optical and X-ray break frequencies in the power spectra of AGN. We introduce the sample, the ASAS-SN and TESS data, and the data analysis procedure in Section 2. We describe the methods for extracting and fitting the PSDs in Section 3. In Section 4, we present the resulting break frequencies and examine how they relate to previous results. We discuss the implications in Section 5.

2. DATA

ASAS-SN (Shappee et al. 2014a; Kochanek et al. 2017) began surveying the sky in 2012. After several expansions, it now consists of 20 14-cm telescopes distributed over 5 “units” and can cover the visible sky nightly in good conditions. The two original units initially used the V -band filter. The 3 new units commissioned in 2017 use g -band filters and the original two units switched to g -band in 2018. During the transition, there were approximately 400 days when both V -band and g -band were used. ASAS-SN images have limiting magnitudes of $V \sim 16.5 - 17.5$ and $g \sim 17.5 - 18.5$ depending on lunation, a field of view of 4.5 deg^2 , a pixel scale of $8''0$, and a typical FWHM of ~ 2 pixels.

Launched in 2018, TESS (Ricker et al. 2015) is equipped with 4 cameras and its TESS bandpass spans a wavelength range of 600 to 1000 nm. Each camera has a field of view of 24° by 24° . The

combined 24° by 96° field of view is called a sector. TESS observes each sector for approximately 27.4 days. For the primary mission, the 26 sectors observed until July 2020, the full-frame images (FFIs) were taken with a 30-minute cadence. The first extended mission, which lasted until September 2022, extending to sector 55, collected FFIs with a 10-minute cadence. In the current, second extended mission, the FFIs are taken with a 200-second cadence. Each sector is divided into two cycles, each lasting for approximately 13 days, with ~ 1 day gap in between for data transmission. The FFIs used for this study can be found in Mikulski Archive for Space Telescopes (MAST; [10.17909/0cp4-2j79](https://mast.stsci.edu/00p4-2j79)).

[González-Martín \(2018\)](#) provided the most recent compilation of AGN with measured X-ray breaks in their power spectra. These AGNs all have *XMM-Newton* observations with 88–1095 ks exposure times. [González-Martín \(2018\)](#) binned the 2–10 keV data into 50-second bins (with a few exceptions using 100- and 200-second bins), and produced light curve segments of 10, 20, 40, 60, 80, and 100 ks. The PSD of each light curve was modeled with a broken power law to measure the break frequency. Each light curve segment for a target was fit separately, leading to a range of break frequency estimates. We compare the optical and X-ray properties of the power spectra of this sample in this paper. Five of these targets (MRK 335, IC 4329A, NGC 5506, ARK 564, and NGC 7469) were not observed by TESS by the end of the first extended mission. For these objects, we use only the ASAS-SN light curves.

2.1. Data reduction

To extract the ASAS-SN light curves, we used image subtraction ([Alard & Lupton 1998](#); [Alard 2000](#)) and aperture photometry (see [Jayasinghe et al. 2018](#) for more details). For calibration, we used the AAVSO Photometric All-Sky Survey (APASS) catalog ([Henden et al. 2015](#)). We corrected the zero-point offsets between different cameras and recalculated the photometric errors as described in [Jayasinghe et al. \(2018\)](#) and [Jayasinghe et al. \(2019\)](#), respectively.

We used a similar method to extract the TESS light curves, with the modifications described in [Fausnaugh et al. \(2021\)](#) and [Vallely et al. \(2021\)](#). We first cut out 750-pixel postage stamps around the target from the FFIs. Then we create a reference image using 100 high-quality images that have no mission-provided data quality flags and have point spread function (PSF) widths and background levels lower than the median values for the sector. We then scale and subtract the reference image from all the individual images. We use a median filtering method to minimize the effects of background structures (the “straps” and complex internal reflection artifacts) and then perform PSF photometry on the subtracted images.

Once the initial TESS light curve is extracted, a few additional adjustments are made. To check for any anomalies, we also extracted light curves for a grid of nearby pixels as shown in [Figure 1](#). At the beginning of each cycle of a TESS Sector, there is often a spike in the backgrounds lasting for a few days. For some objects, this greatly affects the photometry. For example, [Figure 1](#) shows that all the nearby pixels display the same pattern at the beginning of each cycle. The affected segments tend to have greater flux uncertainty, so we computed the median and standard deviation of the flux uncertainty, and took out the portion with uncertainties that deviate significantly from the median. The observations for a sector are interrupted at the middle for data transmission. Sometimes, there is an offset between these two sub-sections (also seen on [Figure 1](#)), which we also correct.

Some sources have anomalous TESS light curves and are discarded. For example, the TESS light curves of 1H 0707–495 ([Figure 2](#)) display a periodic behavior where the flux drops regularly. However, this pattern is observed in most of the nearby pixels, and it is due to a contamination from a nearby

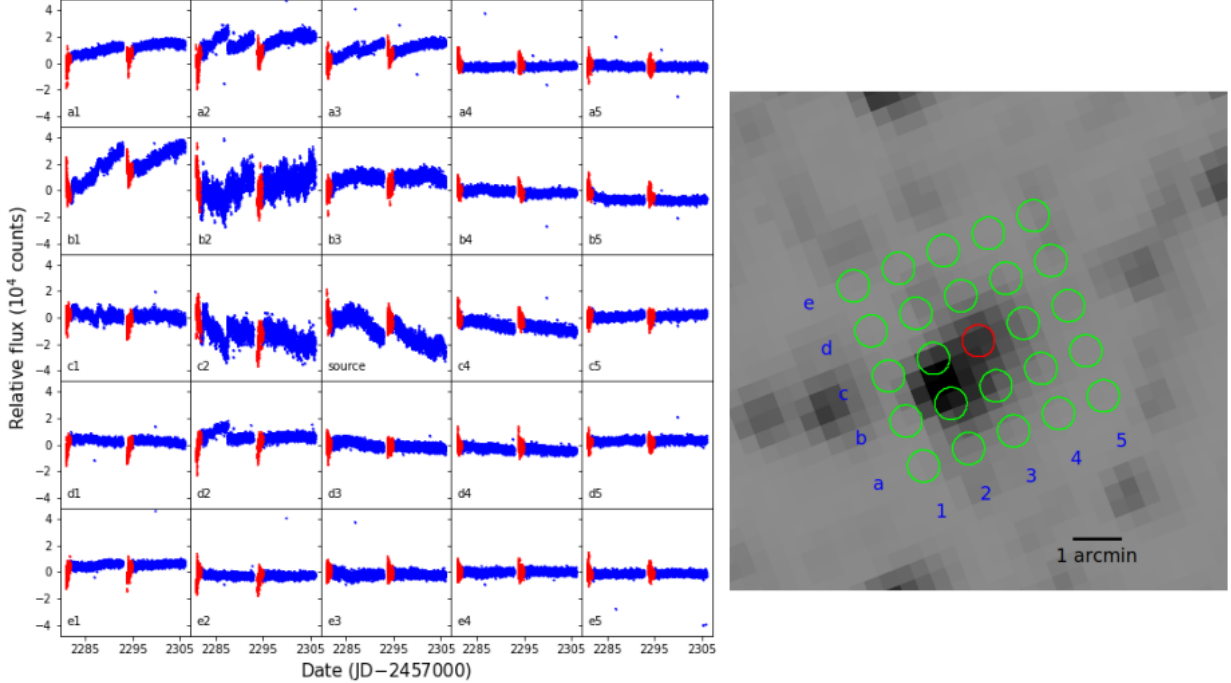


Figure 1. Left: The TESS sector 36 light curve of NGC 3783 and nearby pixels. The center panel labeled “source” is the light curve of the target and the other 24 panels are the light curves of nearby pixels. The red points are the data points with uncertainties greater than the standard deviation of uncertainties from the median of each light curve. Right: The TESS image and the locations of NGC 3783 (red circle) and the nearby pixels (green circles) where the light curves on the left were extracted.

eclipsing binary. All 6 TESS sectors are affected by the binary, so we rejected all the TESS light curves of this target for analysis. We confirmed that there are no other similar cases by checking the ASAS-SN variable stars database (Shappee et al. 2014a; Jayasinghe et al. 2018) for variable stars near each target. Similarly, when we observe unusual features in a TESS light curve, we look at the light curves of nearby pixels to determine if the feature is likely to be real or that the sector should be rejected.

The ASAS-SN light curves are measured in mJy or magnitudes, while the TESS light curves are measured in units of counts relative to the reference frame. Before we extract the power spectra, we converted the TESS light curves into mJy, using the TESS calibration that $1 \text{ count} = 20.44 \pm 0.05 \text{ mag}$ and a zero point of 2631.9 Jy (Vanderspek et al. 2018).

A representative compilation of light curves is shown in Figure 3. It shows that the TESS and ASAS-SN light curves have similar trends with offsets due to the filter differences. The light curves for Circinus are shown in Figure 4. For sectors 11 and 12, a potential sinusoidal pattern was found on nearby pixels affecting the target source’s light curve, while that pattern is not seen in sector 38. So, sectors 11 and 12 were discarded and only sector 38 was used for the PSD analysis.

3. METHODS

3.1. Power spectra

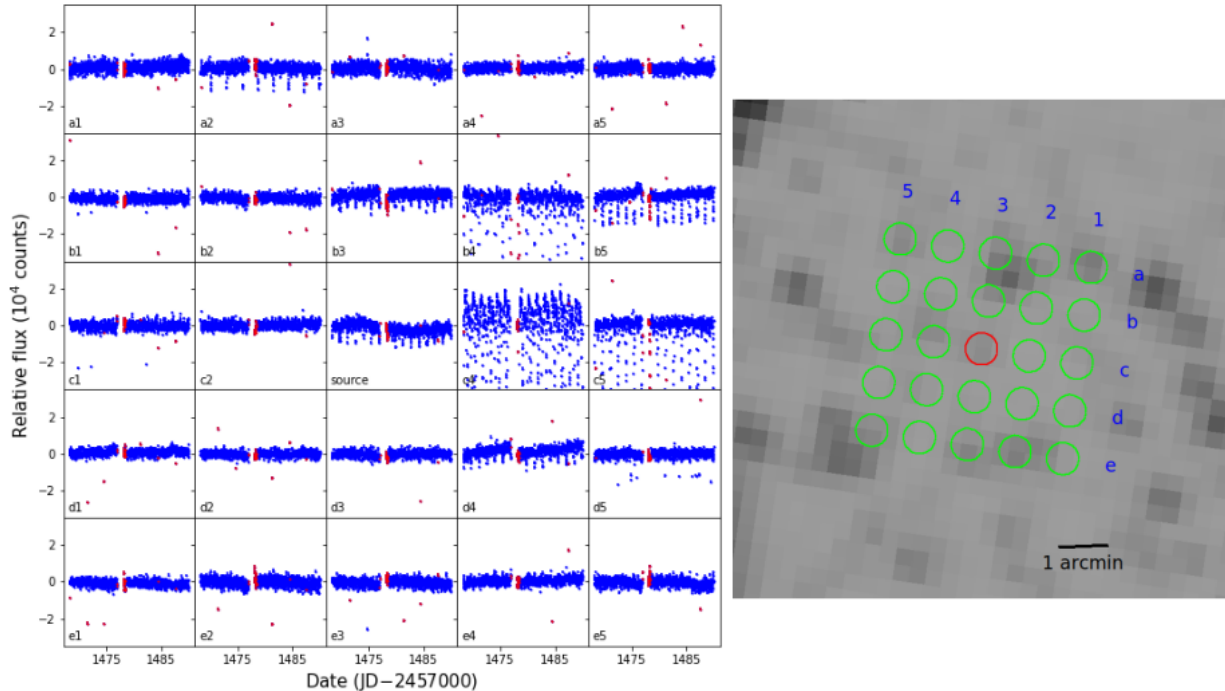


Figure 2. Same as Figure 1 for the TESS sector 6 light curve of 1H 0707-495. The source light curve shows periodic variability due to a nearby eclipsing binary, so this TESS light curve was discarded.

We used a Lomb-Scargle periodogram (Lomb 1976; Scargle 1982) to construct the power spectra. The lower frequency limit is set at $1/T$, where $T = t_N - t_1$ is the time span of the observations, and the upper limit is set at $1/(2\Delta T_{\text{samp}})$, where ΔT_{samp} is the typical sampling interval (1 day for ASAS-SN, 30 minutes for TESS sectors ≤ 26 , 10 minutes for TESS sectors > 26). The raw periodograms from the different data sets do not line up perfectly, so we apply several corrections. First, we apply the rms normalization $2\Delta T_{\text{samp}}/\bar{x}^2 N$ (e.g., Vaughan et al. 2003), where \bar{x} is the mean flux. Such rms normalizations will also minimize the biases due to the filter differences of the different datasets, assuming that the wavelength-dependent AGN variability mainly manifests in the rms amplitudes (e.g., MacLeod et al. 2010). We next separately normalized the PSDs between the ASAS-SN V - and g -band PSDs, and between the multiple TESS sectors' PSDs. There can be additional offsets between ASAS-SN and TESS PSD measurements such as differences in the rms variability between wavelengths. It is challenging to normalize the ASAS-SN and TESS PSDs because the ASAS-SN PSDs are dominated by noise in the overlapping region. We treat this normalization difference in the fitting process. Figure 5 shows an example of the periodograms before and after the scalings.

Before fitting, the periodogram is binned and averaged linearly into logarithmic frequency bins with a width of a factor of 1.6 (0.2 dex) in frequency. The uncertainties are the standard deviations about the mean. To estimate any additional systematic error contribution, we fit a simple power law plus white noise model, $P(\nu) = A\nu^{-\alpha} + C$, calculated the reduced χ^2 statistic, χ_{red}^2 , and then scaled the uncertainties to make χ_{red}^2 unity. On average, χ_{red}^2 before accounting for systematic uncertainties is about 5 for the TESS data, 25 for the V -band ASAS-SN data, and 10 for the g -band ASAS-SN data.

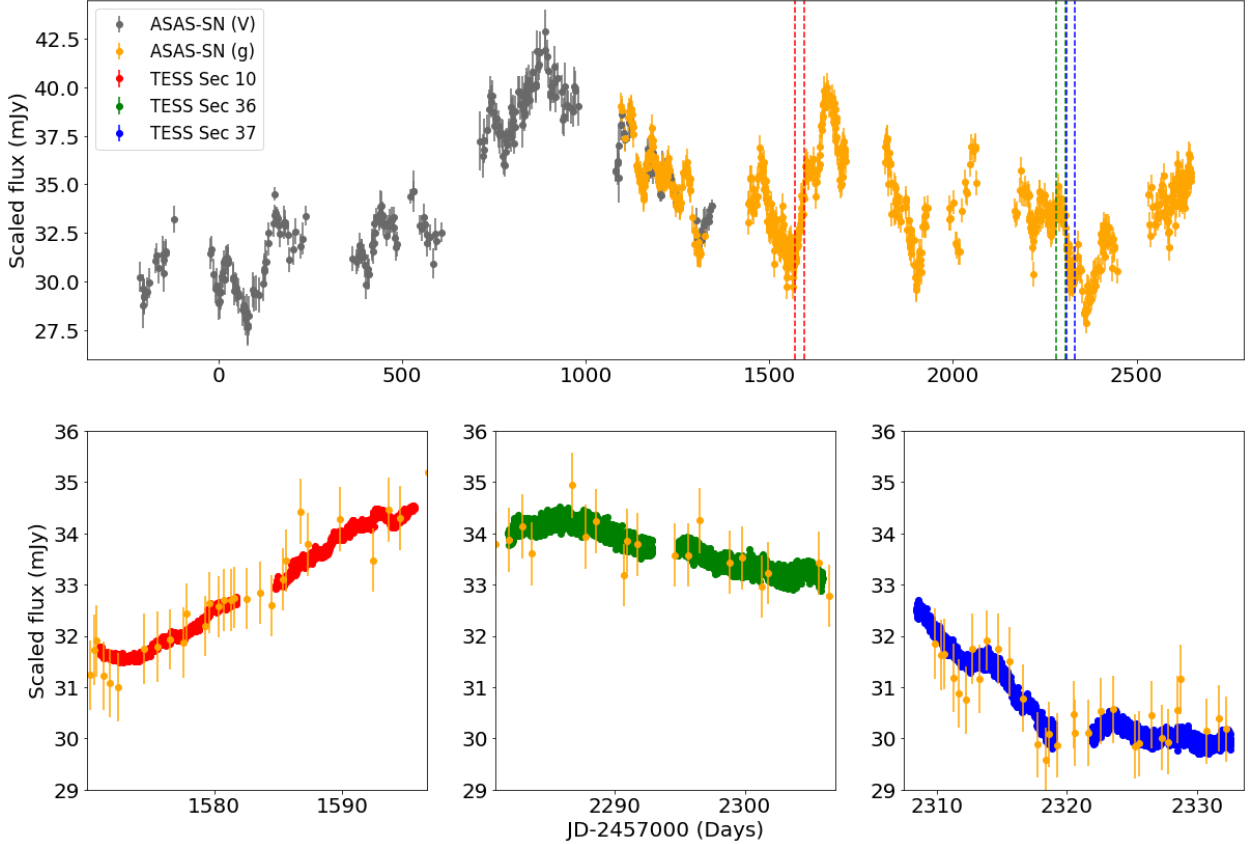


Figure 3. Top: The ASAS-SN light curves of NGC 3783 with the TESS sectors marked. Bottom: TESS light curves along with ASAS-SN data. The light curves are scaled to overlap.

Figure 6 shows an example of the binned periodograms with and without the additional systematic uncertainties.

3.2. Fitting

We fit two models to the periodogram, the broken power law and damped random walk (DRW) models. The main difference between the two models is that the low-frequency and high-frequency power indices are not fixed at 0 and -2 , respectively, in the broken power law model. We first fit a broken power law plus white noise model. Compared to the DRW model, this model has several additional parameters, so we approach the fit in several steps. First, we fit the simple power-law with white noise model, $P(\nu) = A\nu^{-\alpha} + C$ to the individual data sets. Using those fit parameters as initial guesses, the combined periodograms are fit with the smoothly broken power-law plus white noise power spectrum,

$$P(\nu) = A_i \left(\frac{\nu}{\nu_{\text{br}}} \right)^{-\alpha_1} \left\{ \frac{1}{2} \left[1 + \left(\frac{\nu}{\nu_{\text{br}}} \right)^{1/\Delta} \right] \right\}^{(\alpha_1 - \alpha_2)\Delta} + C_i, \quad (1)$$

where ν_{br} is the break frequency, A_i is the amplitude at ν_{br} , α_1 and α_2 are the low and high frequency slopes, respectively, Δ is the smoothness parameter, where the larger values of Δ mean smoother break, and C_i is the noise level for light curve i . Parameters ν_{br} , α_1 , α_2 , and Δ are the same for all PSDs, while the amplitude A_i and noise C_i are different for each data set. The adjustment in the

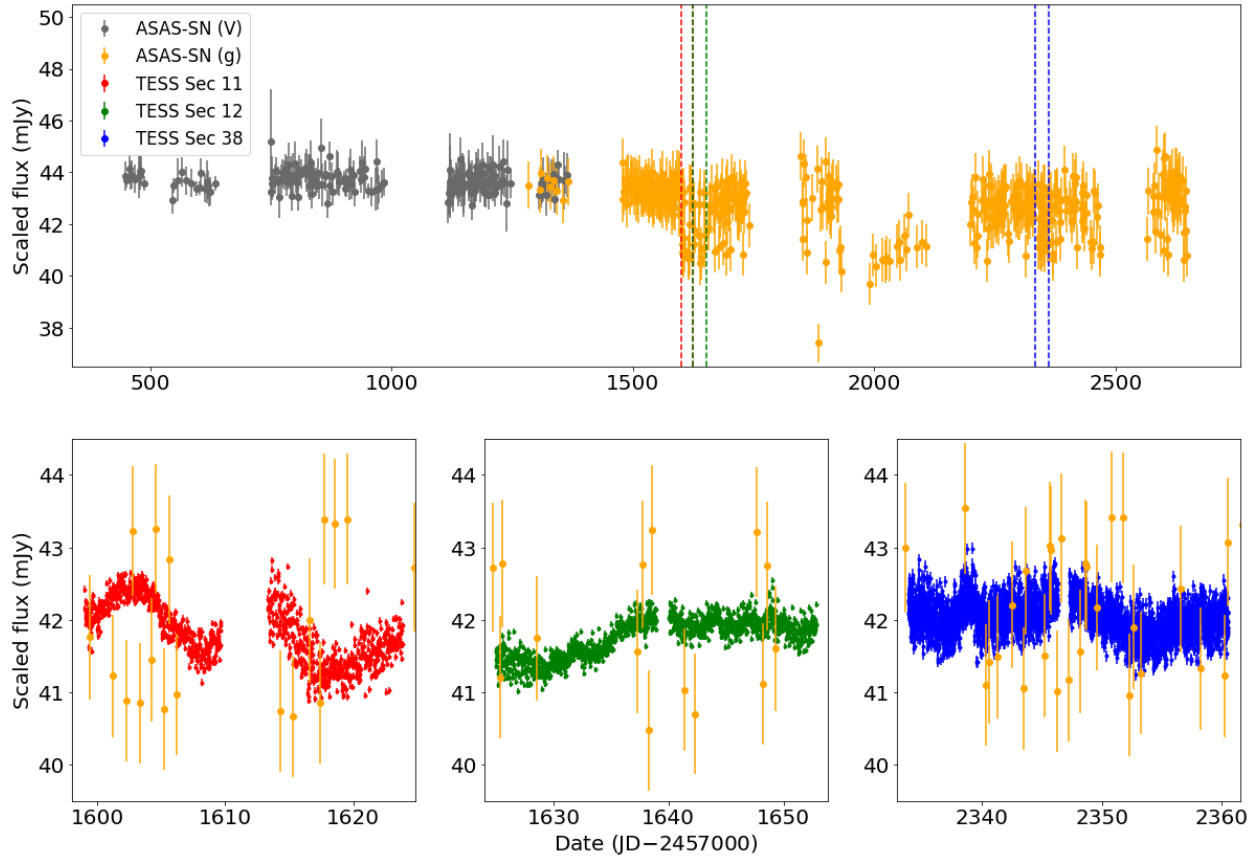


Figure 4. Same as Figure 3 for Circinus with TESS sectors 11, 12, and 38.

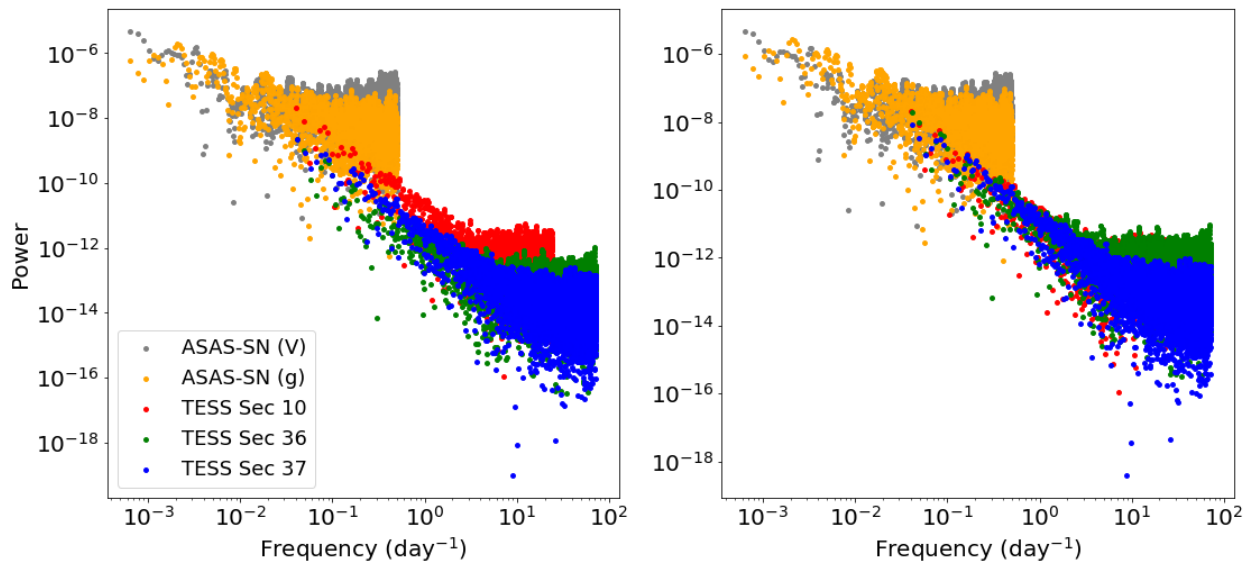


Figure 5. Lomb-Scargle periodogram of NGC 3783 with rms normalization (left), and after additional scaling to line up the PSD (right).

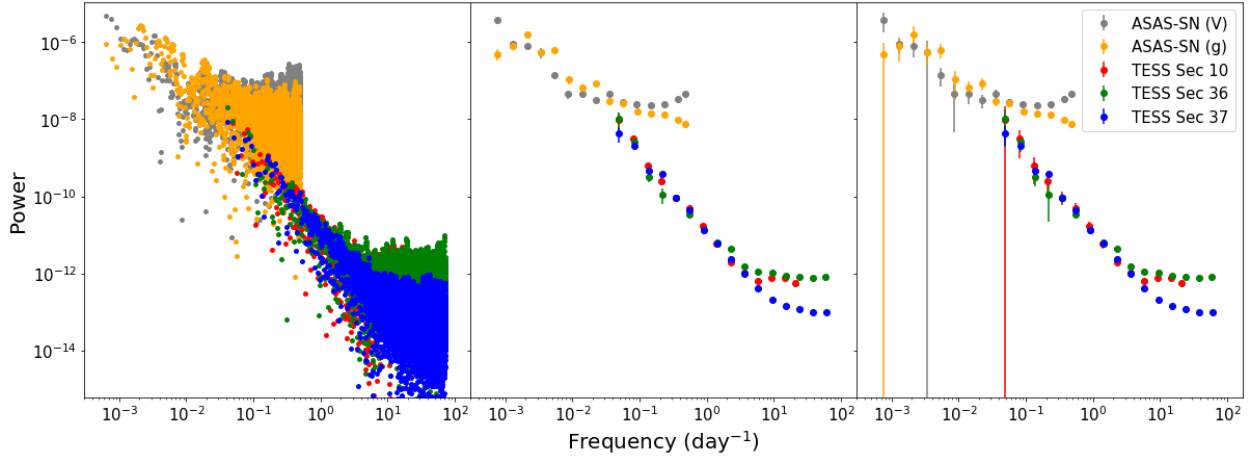


Figure 6. The unbinned periodogram of NGC 3783 (left), the binned periodogram with the standard deviation of the mean as the uncertainty (middle), and the binned periodogram with the additional estimated systematic uncertainties (right).

amplitude allows us to account for any remaining normalization differences between different PSD measurements. We first made fits with Δ fixed at 0.1, 0.2, 0.3, 0.4, and 0.5 and all other parameters free. We found that $\Delta = 0.1$ resulted in the smallest χ^2 , so we fixed $\Delta = 0.1$ for all subsequent fits. Next, we fit the data on a fixed grid of ν_{br} . The frequency at the χ^2 minimum are used as the initial guess for the model, with a $\pm 10\%$ prior constraint on the frequency. Because there are still many parameters to fit, we used the shared value of the amplitude. There are two χ^2 minima in some cases, as shown by the example in Figure 7. For these, we separately tried fits at both minima. After this fit, the constant terms C_i are constrained, to be within $\pm 10\%$ of the values from previous fit and the amplitudes A_i are allowed to vary independently. For the final fit, we constrained the amplitudes A_i and noise terms C_i to be within 10% of the prior trial fit values and allow the power law indices to be free parameters.

From the broken power law fits, we find two sets of break frequencies, low- and high-frequency breaks with the dividing line at around 10^{-2} day^{-1} . The low frequency breaks $\nu_{\text{br,low}}$ are measured in objects with only ASAS-SN data, joint fits with TESS and ASAS-SN with a single χ_{red}^2 minimum below 10^{-2} day^{-1} , as well as the low frequency χ_{red}^2 minimum for joint fits with two χ_{red}^2 minima. These break frequencies and their associated slopes are similar to those from the DRW fits discussed below, meaning that the break frequencies are close to DRW break frequencies and power law indices are about $\alpha_1 = 0$ and $\alpha_2 = 2$. The high frequency breaks $\nu_{\text{br,hig}}$, meaning a χ_{red}^2 minimum at frequencies higher than 10^{-2} day^{-1} , are prominent in most targets with both ASAS-SN and TESS data. These $\nu_{\text{br,hig}}$ are typically in the overlapping region of the ASAS-SN and TESS power spectra. For ASAS-SN, the PSDs at these frequencies are dominated by white noise. For the fits yielding $\nu_{\text{br,hig}}$, the power law indices for the low and high frequencies deviate from 0 and 2, especially the low-frequency slopes α_1 (Figure 8).

We also fit the DRW model, also known as the continuous time first-order autoregressive (CAR(1)) process (e.g., Kelly et al. 2009), plus white noise. The DRW model has the power spectrum

$$P(\nu) = \frac{2\sigma^2\tau^2}{1 + (2\pi\tau\nu)^2}, \quad (2)$$

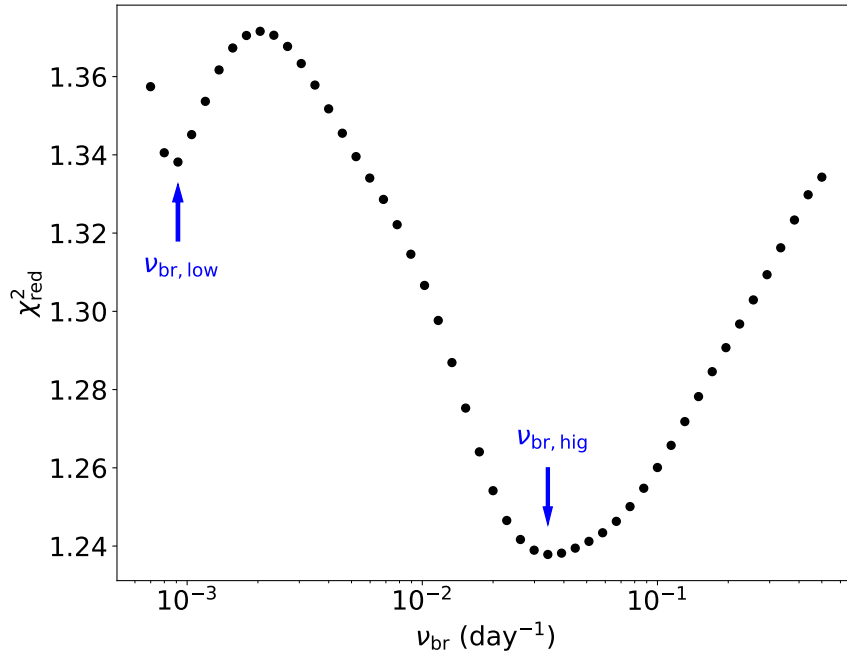


Figure 7. The reduced chi squared for the broken power law model fitting as a function of the break frequencies for MRK 766. The positions we identify as the two break frequencies are labeled.

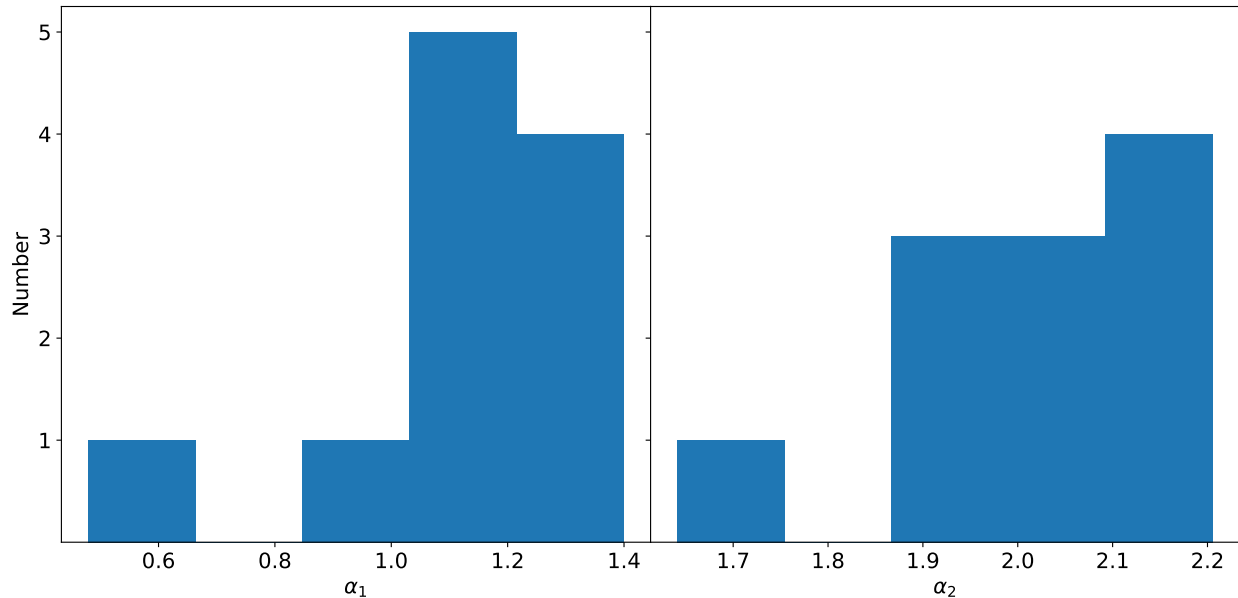


Figure 8. Distribution of the low-frequency (left, α_1) and high-frequency (right, α_2) slopes for the broken power law fits using $\nu_{\text{br,hig}}$.

where σ is the characteristic timescale and τ is the relaxation time. The relaxation time τ defines the break frequency of $\nu_{\text{br}} = 1/2\pi\tau$. Since most previous optical PSD studies did not use light curves with the high cadence of TESS, we fit the DRW model to both the separate and combined ASAS-SN and TESS PSDs. In general, the DRW fits yield break frequencies in the ASAS-SN frequency regime, which is consistent with previous studies.

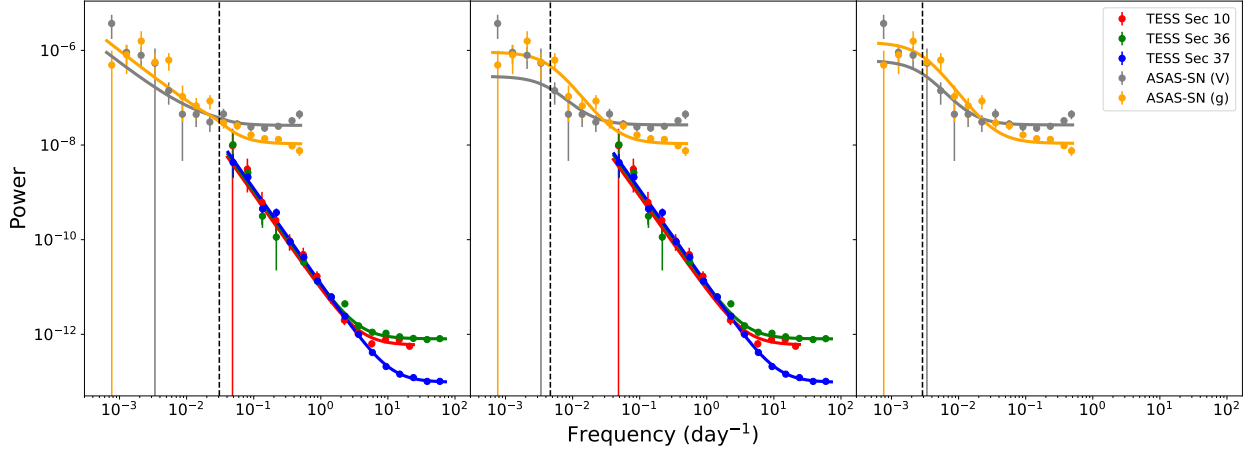


Figure 9. The binned periodogram of NGC 3783 fit with a broken power law with the high break frequency (left), a DRW using both TESS and ASAS-SN data (middle), and using only the ASAS-SN (right), The vertical dashed lines mark the break frequencies.

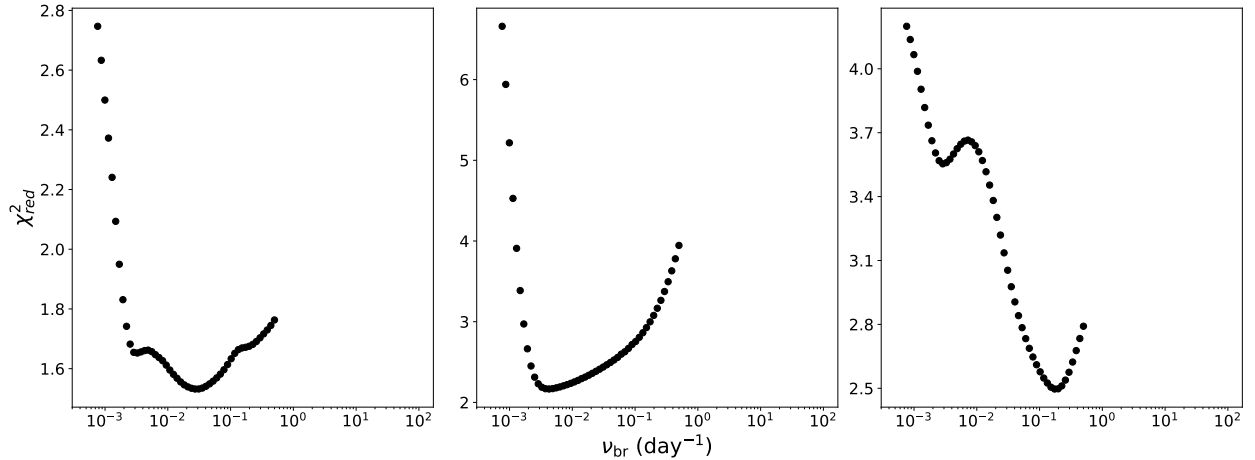


Figure 10. Reduced chi squared as a function of break frequency for the three fits shown in Figure 9. There are two minima for the DRW fit to the ASAS-SN PSDs, but the minimum at the higher frequency is in the noise-dominated region, so the low-frequency break is used.

3.3. Comparison between Long-term ASAS-SN and TESS Light Curves and PSDs

Since most of the high-frequency breaks lie in the overlapping frequency range of the TESS and ASAS-SN PSDs, it is important to compare TESS and ASAS-SN light curves and PSDs on these time scales for potential calibration issues or variability characteristic differences between filters. Typical TESS Sectors are too short for this purpose. However, TESS observes the ecliptic poles continuously for 13 sectors, so it is possible to extract long-term, nearly continuous TESS light curves for objects near the poles. For this analysis, we used PG 1613+658, a Seyfert I galaxy near the North ecliptic pole observed over Sectors 14 to 26 during the primary mission. The combined light curve is shown in Figure 11.

We constructed the PSD for the combined TESS light curve using the same procedures to examine if the low-frequency regime of the combined TESS PSDs is consistent with those measured by ASAS-

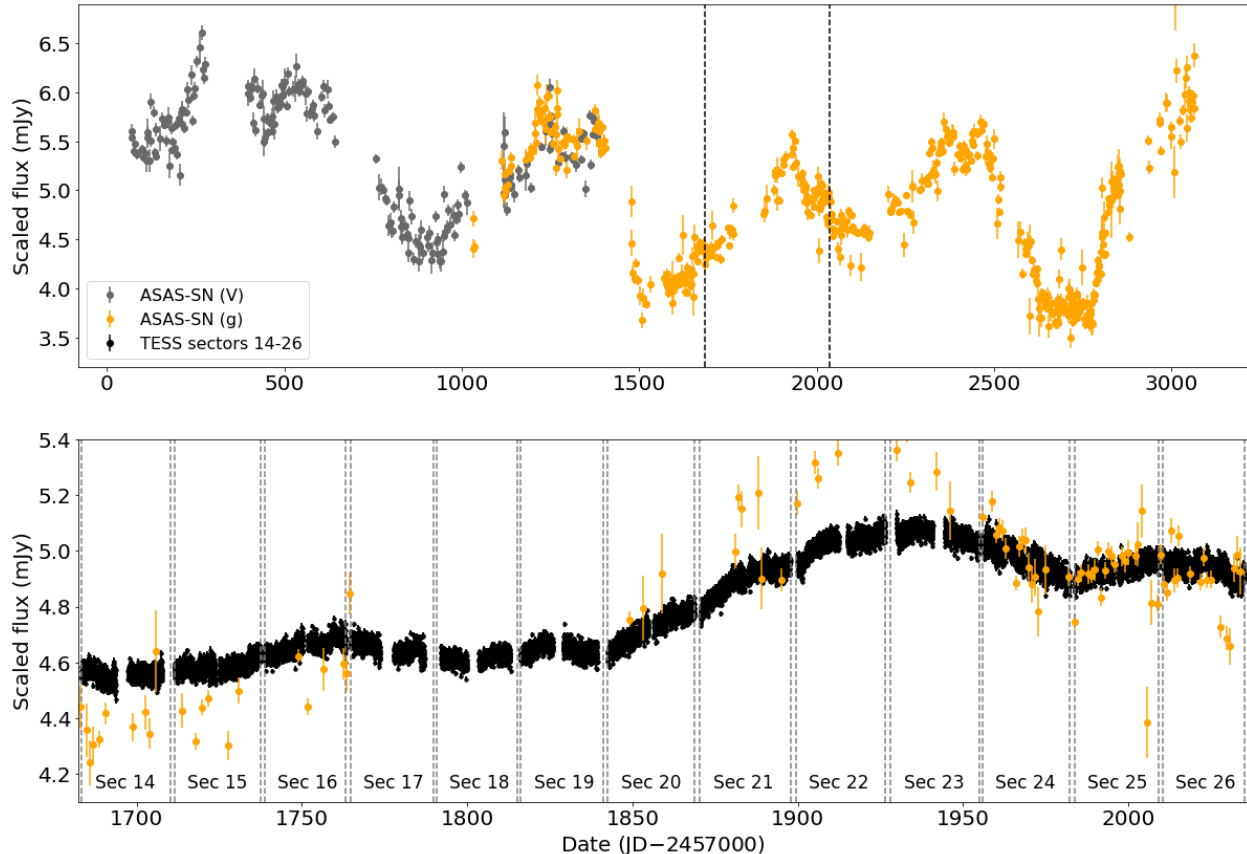


Figure 11. Top: The ASAS-SN light curve of PG 1613+658 with the observation window of PG 1613+658 during the TESS primary mission marked. Bottom: The TESS primary mission light curve of PG 1613+658 along with the ASAS-SN g-band data. The vertical dashed lines are the sector boundaries.

SN, up to a normalization difference. To do so, we estimated and subtracted the white noise of each PSD. We compare the PSDs of the continuous TESS light curve, the PSDs of ASAS-SN V-band and g-band light curves, and the average of the 13 PSDs for the individual TESS sectors in Figure 12, finding that the TESS and ASAS-SN PSDs are consistent in the overlapping regions and have similar slopes at low frequencies. We did not use the PSD from all 13 sectors because it has strong artificial peaks at $14n$ ($n = 1, 2, 3, \dots$) days created by the observing cadence that strongly affect the fits to the PSD. The results for the broken power law PSD fits are shown in Figure 13. Only one break frequency is found at $\log(\nu_{\text{br}}/\text{day}^{-1}) = -1.02 \pm 0.09$ which is within the typical range of $\nu_{\text{br,high}}$ of the AGN sample.

4. RESULTS

We have 2 estimates of the low frequency break from the DRW models (PSD models for either the ASAS-SN or the ASAS-SN plus TESS data), and a set of low and high frequency breaks from the broken power law fits to the ASASS-SN plus TESS PSDs. All breaks related to the DRW models are in the low frequency regime. We compare these breaks with the X-ray break frequencies and black hole masses from González-Martín (2018) in Figures 14, 15, and 16. González-Martín (2018) only list the range of X-ray break frequencies found for their X-ray light curve segments, so we used the midpoint and the range of the values as the X-ray break frequencies and their uncertainties.

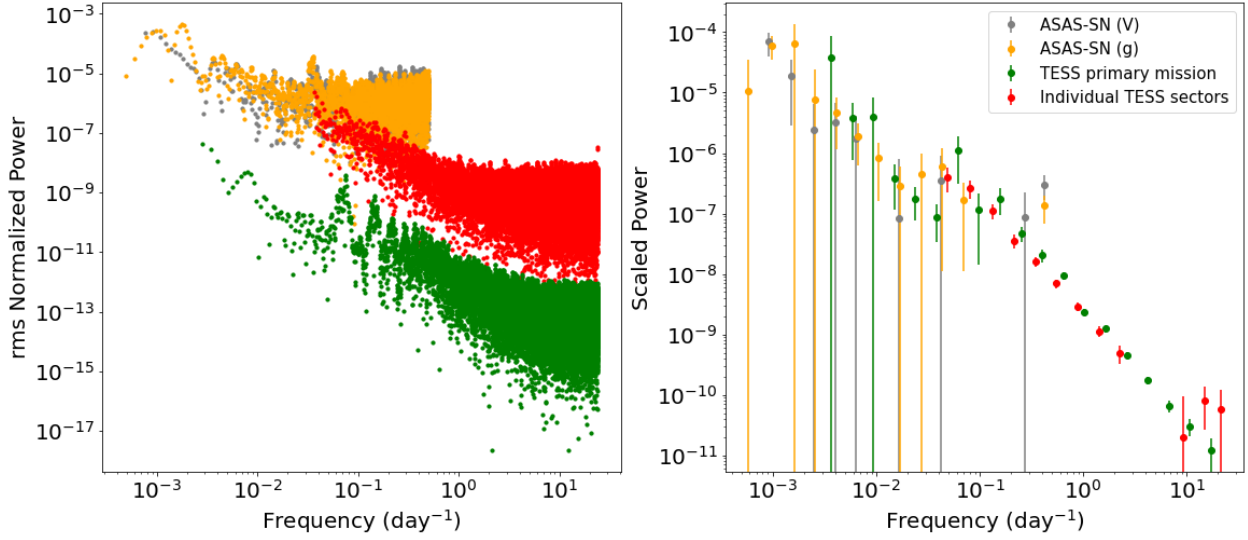


Figure 12. Left: The rms normalized PSDs of PG 1613+658. The PSD in green is constructed using the continuous 13 sector TESS light curve, while the red is the collection of the individual sector PSDs. Right: The binned PSDs with the white noise level subtracted and scaled to line up. The individual TESS sector PSDs are averaged before being binned.

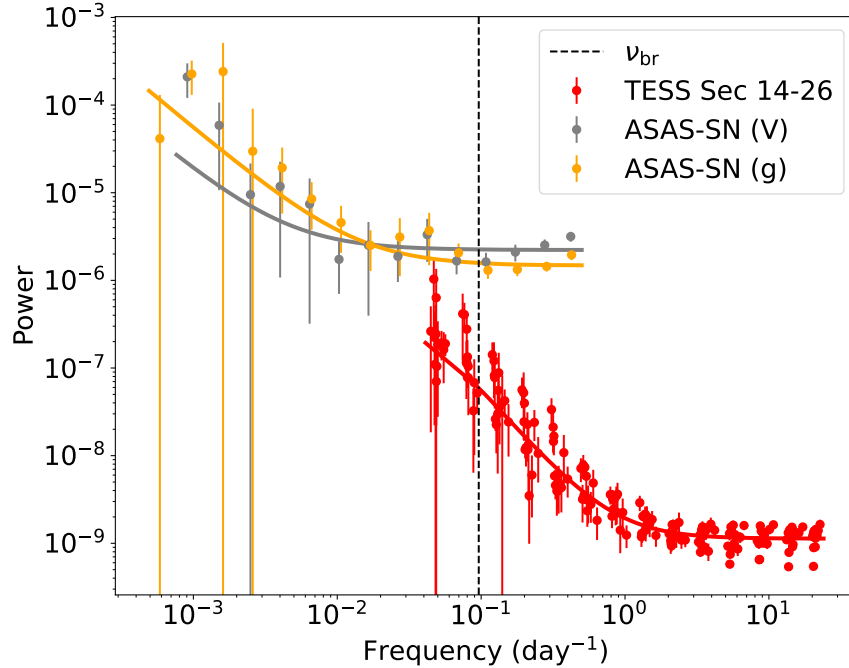


Figure 13. The PSDs with the broken power law fit of PG 1613+658. The PSDs in red labeled TESS sectors 14-26 are the PSDs of the individual sectors.

To test the relationship between the optical break frequencies and black hole mass and X-ray break frequencies, we computed Pearson's correlation coefficient (Table 1). We discuss the low and high frequency regimes separately.

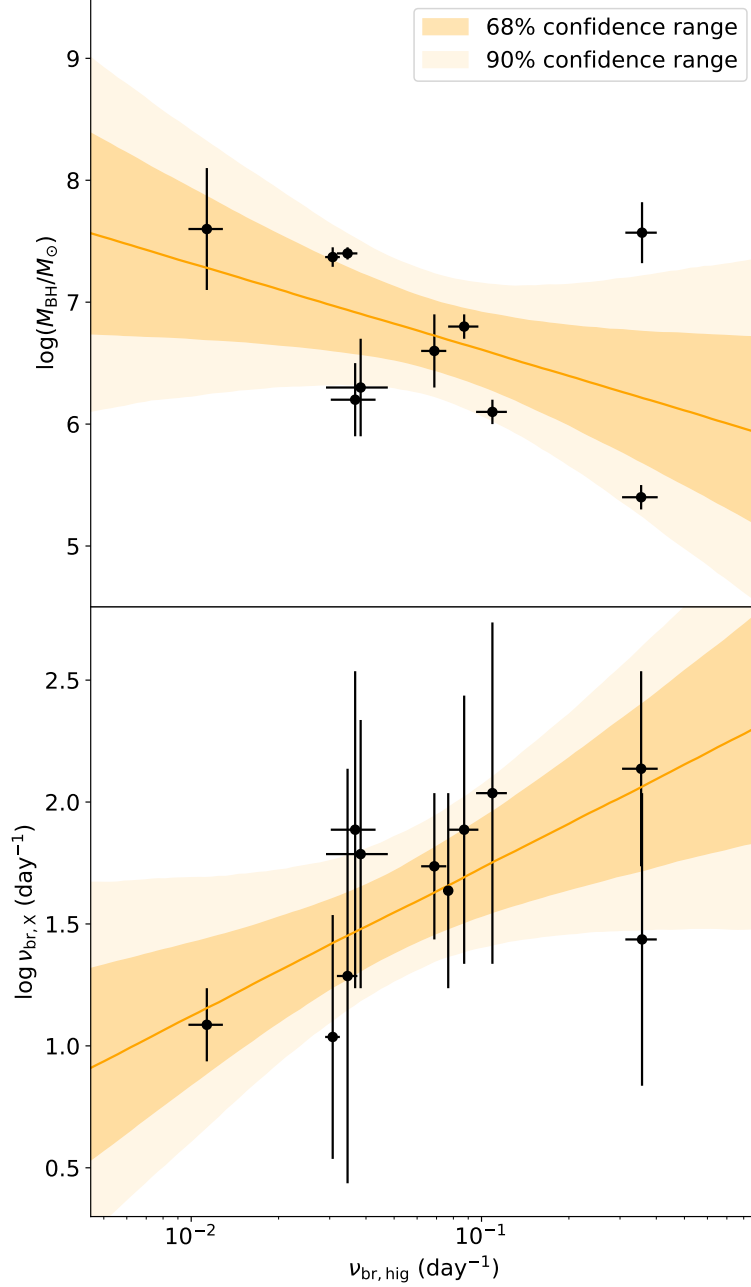


Figure 14. Black hole mass and X-ray break frequency versus the high optical break frequencies along with linear fits and their uncertainties.

4.1. High-Frequency Optical Breaks

The high frequency optical breaks were detected in the broken power law fits to the combined ASAS-SN and TESS PSDs. They are all at frequencies above 10^{-2} day^{-1} , and resemble the steepening of optical PSDs found in Kepler data (Mushotzky et al. 2011; Kasliwal et al. 2015; Aranzana et al. 2018; Smith et al. 2018). Here, we can compare them with the X-ray break frequencies measured for the same set of objects. The high-frequency optical $\nu_{\text{br,hig}}$ and X-ray $\nu_{\text{br,X}}$ break frequencies are given in Table 2 along with M_{BH} and shown in Figure 14. The ranked correlation test shows that the high

frequency optical breaks and X-ray breaks are significantly correlated with a null probability of 7%. We also found a hint of correlation between the high frequency breaks and the black hole masses, but at lower significance. Figure 14 shows fits to the correlations using

$$\log\left(\frac{\nu_{\text{br,X}}}{\text{day}^{-1}}\right) = \beta_1 \log\left(\frac{\nu_{\text{br,hig}}}{10^{-1}\text{day}^{-1}}\right) + \delta_1 \quad (3)$$

and

$$\log\left(\frac{M_{\text{BH}}}{M_{\odot}}\right) = \beta_2 \log\left(\frac{\nu_{\text{br,hig}}}{10^{-1}\text{day}^{-1}}\right) + \delta_2. \quad (4)$$

to find that $\beta_1 = 0.59_{-0.34}^{+0.33}$, $\delta_1 = 1.71_{-0.18}^{+0.19}$, $\beta_2 = -0.70_{-0.66}^{+0.68}$, and $\delta_2 = 6.61_{-0.30}^{+0.31}$.

Burke et al. (2020) performed a similar break frequency analysis on NGC 4395. They used the TESS sector 22 light curve to construct the PSD and fit a broken power law. They found a break frequency of $\log(\nu_{\text{br}}/\text{day}^{-1}) = -0.94 \pm 0.25$, which differs from our value of $\log(\nu_{\text{br}}/\text{day}^{-1}) = -0.48 \pm 0.11$. This may be due to using both TESS and ASAS-SN data. Using only the TESS PSDs, we find $\log(\nu_{\text{br}}/\text{day}^{-1}) = -0.93 \pm 0.07$, which agrees with Burke et al. (2020).

Another target in the high frequency break sample, PG 1613+658, the Seyfert I galaxy with 13 continuous TESS sectors discussed earlier, was not included in these fits because it does not have a reported X-ray break frequency. It does have a reverberation mapping black hole mass measurement of $\log(M_{\text{BH}}/M_{\odot}) = 8.38_{-0.16}^{+0.25}$ (Kaspi et al. 2000). Using the break frequency from the PSD of the continuous TESS light curve and the $M_{\text{BH}}-\nu_{\text{br}}$ relationship (Equation 4), we get $\log(M_{\text{BH}}/M_{\odot}) = 6.62_{-1.01}^{+0.99}$. Though the difference in the central values is large, the two values agree within 2σ because of the large uncertainties in the correlation.

We find that the slopes of the broken power law fits do not have a strong correlation with the black hole mass or the break frequency. The Pearson’s correlation test parameters are $r = -0.17$ and $p = 0.63$ for $\alpha_1 - M_{\text{BH}}$, $r = 0.33$ and $p = 0.32$ for $\alpha_1 - \nu_{\text{br,hig}}$, $r = -0.38$ and $p = 0.28$ for $\alpha_2 - M_{\text{BH}}$, and $r = -0.22$ and $p = 0.51$ for $\alpha_2 - \nu_{\text{br,hig}}$ pairs.

4.2. Low-Frequency Optical Breaks

From the three sets of low-frequency optical breaks, we focus on those from the broken power law fits, since they correlate better with the black hole mass and X-ray breaks of the sample. We also compare our results to scaling relations between the low frequency break and black hole mass from Kelly et al. (2009), MacLeod et al. (2010), and Burke et al. (2021). To compare with the multivariate correlation MacLeod et al. (2010), we use their relations assuming a rest frame wavelength of $\lambda_{\text{RF}} = 8000\text{\AA}$, an absolute magnitude of $M_i = -21.3$, and a redshift of $z = 0.02$. All three relations are shown in Figures 15 and 16.

The ranked correlation test shows that the low frequency break from the broken power law fits correlate with both the black hole mass and the X-ray break frequencies with null probabilities of 0.06 and 0.10, respectively. The break versus black hole mass relation is quite consistent with previous relations (Figure 15). We fit the relationships using

$$\log\left(\frac{\nu_{\text{br,X}}}{\text{day}^{-1}}\right) = \beta_3 \log\left(\frac{\nu_{\text{br,low}}}{10^{-1}\text{day}^{-1}}\right) + \delta_3 \quad (5)$$

and

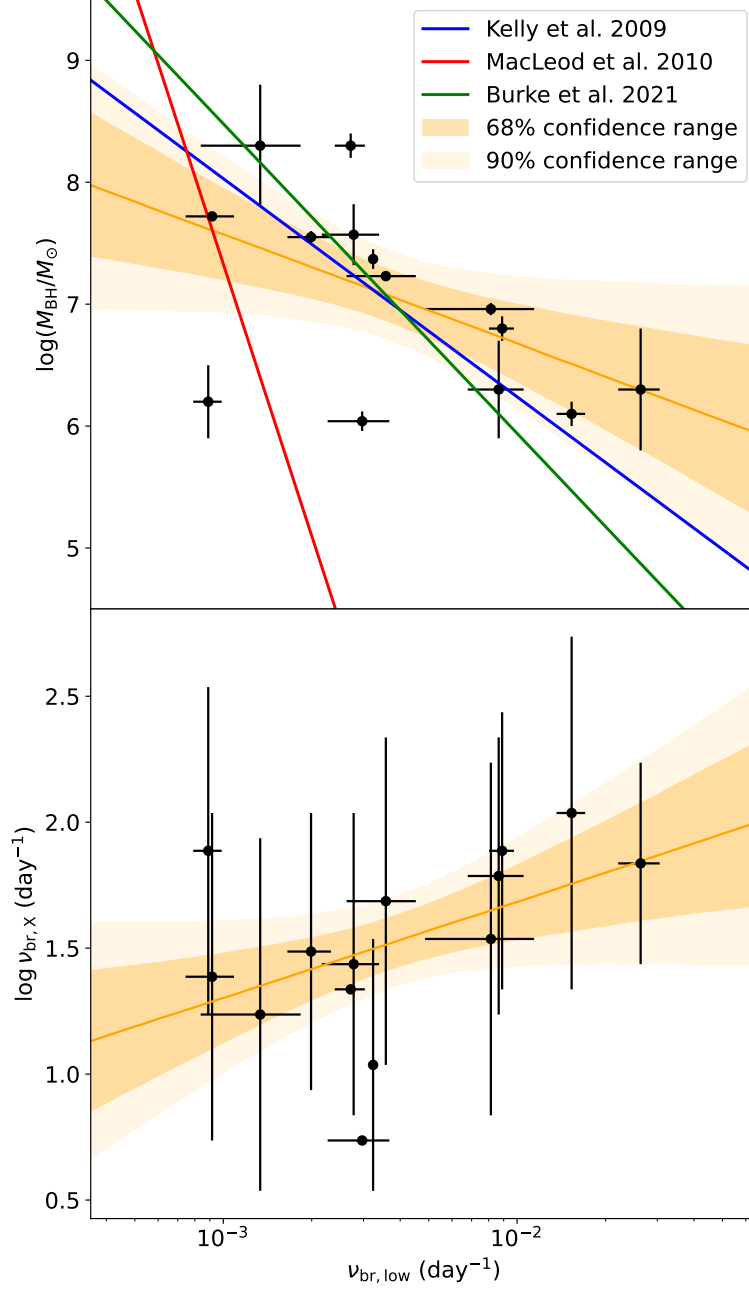


Figure 15. X-ray break frequency $\nu_{\text{br,X}}$ and M_{BH} versus low optical break frequency $\nu_{\text{br,low}}$ with the best linear fit and its uncertainties. The upper panel shows similar fits from Kelly et al. (2009), MacLeod et al. (2010), and Burke et al. (2021).

$$\log\left(\frac{M_{\text{BH}}}{M_{\odot}}\right) = \beta_4 \log\left(\frac{\nu_{\text{br,low}}}{10^{-1}\text{day}^{-1}}\right) + \delta_4. \quad (6)$$

We find that $\beta_3 = 0.38_{-0.25}^{+0.25}$, $\delta_3 = 2.06_{-0.37}^{+0.38}$, $\beta_4 = -0.90_{-0.52}^{+0.52}$, and $\delta_4 = 5.79_{-0.77}^{+0.76}$, with the results shown in Figure 15.

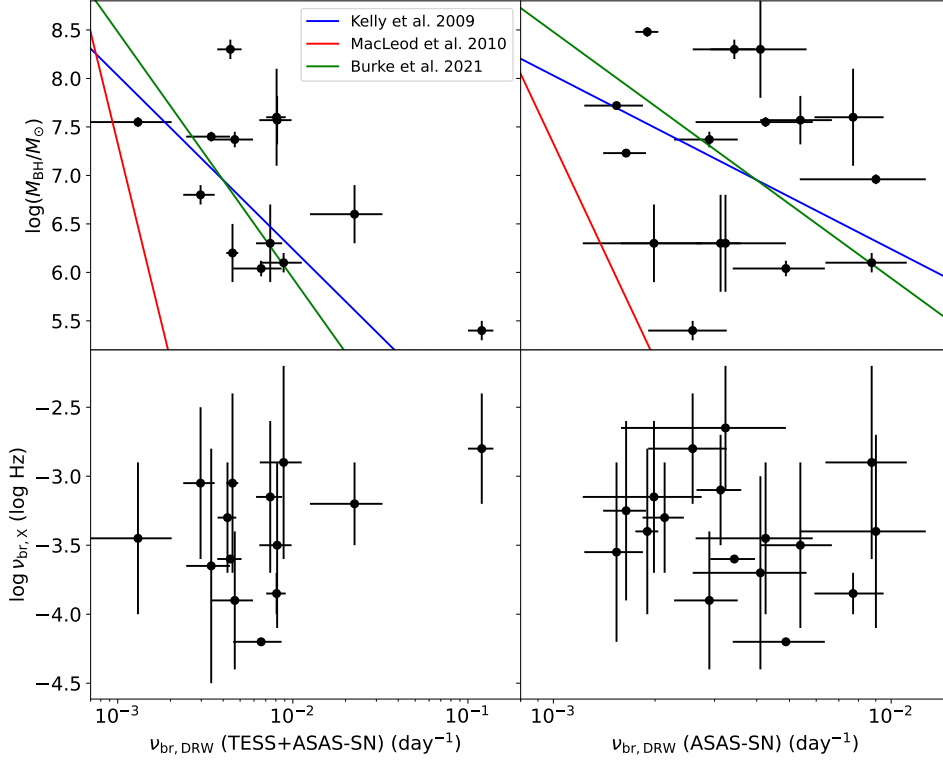


Figure 16. $\nu_{\text{br},X}$ and M_{BH} versus $\nu_{\text{br}} = 1/(2\pi\tau)$ from DRW model fit on TESS and ASAS-SN PSDs (left), and on ASAS-SN PSDs only (right).

Table 1. Pearson correlation coefficients

ν_{br} from	M_{BH}		$\nu_{\text{br},X}$	
	r	p	r	p
BPL fit with high break frequency	-0.41	0.23	0.57	0.07
BPL fit with low break frequency	-0.52	0.06	0.45	0.10
DRW fit with all data	-0.60	0.03	0.37	0.19
DRW fit with ASAS-SN data	-0.12	0.66	-0.17	0.51
JAVELIN with all data	-0.50	0.17	0.43	0.25
JAVELIN with ASAS-SN data	-0.28	0.22	0.30	0.18

The $\nu_{\text{br}} - M_{\text{BH}}$ relationship found using the various DRW fits do not agree with previous studies very well, though the DRW PSD fits using both TESS and ASAS-SN have a similar trend (Figure 16). Although the correlations between these DRW break frequencies and X-ray break frequencies are not significant, as can be seen in the bottom panels in Figure 16, the X-ray break dependence on the DRW breaks is almost flat, confirming the shallow slope ($\beta_3 = 0.38 \pm 0.25$) between the low frequency breaks from the broken power law model and X-ray breaks.

Table 2. Properties of the AGN sample

Name	TESS sectors	$\log(M/M_{\odot})$	$\log \nu_{\text{br},X}$ (Hz)	$\log \nu_{\text{br},\text{DRW}}$ (day^{-1})	$\log \nu_{\text{br},\text{low}}$ (day^{-1})	$\log \nu_{\text{br},\text{high}}$ (day^{-1})
MRK 335	N/A	7.23 ± 0.04	[-3.9,-2.6]	-2.78 ± 0.06	-2.45 ± 0.12	N/A
ESO 113-G010	1, 2, 28, 29	N/A	[-3.7,-2.9]	-2.67 ± 0.06	N/A	-1.11 ± 0.02
Fairall 9	2, 28, 29	8.3 ± 0.1	-3.6	-2.46 ± 0.07	-2.57 ± 0.05	N/A
PKS 0558-504	1*, 5, 6, 7, 11*, 32, 33, 34	8.48 ± 0.05	[-4.0,-2.8]	-2.72 ± 0.03	N/A	N/A
1H0707-495	6*, 7*, 8*, 33*, 34*, 35*	6.3 ± 0.5	[-3.5,-2.7]	-2.51 ± 0.07	-1.58 ± 0.07	N/A
ESO 434-G040	9, 35	7.57 ± 0.25	[-4.1,-2.9]	-2.27 ± 0.10	-2.56 ± 0.10	-0.45 ± 0.05
NGC 3227	45, 46, 48	6.8 ± 0.1	[-3.6,-2.5]	N/A	-2.05 ± 0.04	-1.06 ± 0.05
REJ 1034+396	21, 48	6.6 ± 0.3	[-3.5,-2.9]	N/A	N/A	-1.16 ± 0.04
NGC 3516	14, 20, 21, 41, 47, 48	7.40 ± 0.05	[-4.5,-2.8]	N/A	N/A	-1.46 ± 0.04
NGC 3783	10, 36, 37	7.37 ± 0.08	[-4.4,-3.4]	-2.54 ± 0.09	-2.49 ± 0.01	-1.51 ± 0.03
NGC 4051	22, 49	6.1 ± 0.1	[-3.6,-2.2]	-2.06 ± 0.12	-1.81 ± 0.05	-0.96 ± 0.05
NGC 4151	49	7.55 ± 0.05	[-4.0,-2.9]	-2.37 ± 0.16	-2.70 ± 0.07	N/A
MRK 766	22	6.2 ± 0.3	[-3.7,-2.4]	N/A	-3.05 ± 0.05	-1.44 ± 0.08
NGC 4395	22, 49	5.4 ± 0.1	[-3.2,-2.4]	-2.59 ± 0.11	N/A	-0.45 ± 0.06
MCG-06-30-15	11*, 37	6.3 ± 0.4	[-3.7,-2.6]	-2.70 ± 0.17	-2.06 ± 0.09	-1.42 ± 0.10
IC 4329A	N/A	8.3 ± 0.5	[-4.4,-3.0]	-2.39 ± 0.16	-2.87 ± 0.16	N/A
Circinus	11*, 12*, 38	6.04 ± 0.08	[-4.2,-4.2]	-2.31 ± 0.13	-2.53 ± 0.10	N/A
NGC 5506	N/A	8.1 ± 0.2	[-3.9,-2.8]	N/A	N/A	N/A
NGC 5548	23, 50	7.72 ± 0.02	[-4.2,-2.9]	-2.81 ± 0.09	-3.04 ± 0.08	N/A
NGC 6860	13, 27	7.6 ± 0.5	[-4.0,-2.9]	-2.11 ± 0.10	N/A	-1.95 ± 0.06
ARK 564	N/A	6.3 ± 0.5	[-3.1,-2.2]	-2.49 ± 0.22	N/A	N/A
NGC 7469	N/A	6.96 ± 0.05	[-4.1,-2.7]	-2.05 ± 0.18	-2.09 ± 0.18	N/A

NOTE— $\log \nu_{\text{br},\text{DRW}}$ are from fits using ASAS-SN data only. * Discarded data.

5. DISCUSSION

We study AGN variability over six orders of magnitude from minutes to decade time-scales by combining TESS and ASAS-SN light curves. Our analysis shows that the ASAS-SN and TESS PSDs can be jointly modeled with a normalization offset due to differences in noise levels and filters. We analyzed a bright target PG 1613+658 in the TESS continuous monitoring regions, giving it a TESS light curve spanning more than a year, so that there is a significant overlap between PSDs, and found consistent light curves and PSD measurements.

AGN variability PSDs are generally characterized by power laws with breaks, where distinct break frequencies have been observed in both optical (e.g., Kelly et al. 2009; MacLeod et al. 2010; Simm et al. 2016; Burke et al. 2021) and X-ray data (e.g., Uttley et al. 2002; Markowitz et al. 2003; González-Martín & Vaughan 2012; González-Martín 2018). Both the optical and X-ray break frequencies are correlated with the black hole mass, but with quite different scaling relations (e.g., Simm et al. 2016; Burke et al. 2021). The fact that the break frequency and black hole mass have statistically significant correlation suggests that the AGN variability is closely related to accretion physics.

This paper presents the first analysis comparing optical and X-ray PSDs by utilizing the all-sky nature of ASAS-SN and TESS surveys. We find a set of high frequency breaks ($\gtrsim 10^{-2}\text{day}^{-1}$) in the joint optical light curves. These high frequency breaks were previously observed as a steepening of the optical PSD at high frequencies (Mushotzky et al. 2011; Kasliwal et al. 2015; Aranzana et al. 2018; Smith et al. 2018). We find a correlation between the X-ray and high-frequency optical break frequencies. The slope of the power law relation of $\beta_1 = 0.59_{-0.34}^{+0.33}$ is consistent with a simple proportional relation ($\beta_1 = 1$), given the uncertainty. Under this simple proportional relation, we can interpret the offset between the optical and X-ray break frequencies in the linear fit, δ_1 , as the light crossing time between the X-ray and optical emission regions. A slope shallower than unity implies that the X-ray emission region is relatively smaller than the optical for greater M_{BH} . A larger sample is needed to better establish the correlation with more accurate slope measurements.

There is also an indication that the high frequency optical breaks are correlated with the black hole mass, though weakly. This could be a new scaling relationship $\nu_{\text{br}} - M_{\text{BH}}$, different from those found in previous studies, providing an alternative method to estimate the black hole mass.

The X-ray emission is produced from inverse Compton scattering between UV seed photons from the accretion disk and electrons in the corona. The X-ray emission then irradiates the accretion disk, heating the disk and modifying the optical emission. Therefore, the optical and X-ray variability should show correlations. In fact, short timescale correlations between optical and X-ray light curves are well established and used as a tool for continuous reverberation mapping studies to constrain optical and X-ray emission sizes (e.g., Shappee et al. 2014b; Edelson et al. 2015; Troyer et al. 2016; McHardy et al. 2018). The correlation we find between the X-ray and optical PSD break frequencies provides independent support that the optical and X-ray emissions are closely related on short time scales. Since the optical PSD on these scales deviates from the extrapolation from longer time-scales, the variation of the X-ray emission, through “reprocessing”, can be the main driver for the interaction between optical and X-ray emission.

The X-ray emission, which can vary on very short timescales, is speculated to come from the innermost part of the AGN, near the SMBH. On the other hand, the optical emission is believed to come from the accretion disk. Studies in quasar microlensing (e.g., Morgan et al. 2008; Dai et al. 2010) and reverberation mapping (e.g., Shappee et al. 2014b; Edelson et al. 2015; Cackett et al.

2018; Jha et al. 2022) find that the sizes of X-ray and optical emission regions range from 10^{14} to 10^{15} cm and from 10^{15} to 10^{16} cm, respectively. This scale is comparable to our observed difference in characteristic timescales, with $\tau = 1/(2\pi\nu_{\text{br}}) \sim 10^{-2}$ day for the X-rays and $\sim 10^0$ days for the optical.

In the low frequency regime ($\lesssim 10^{-2}\text{day}^{-1}$), we also found a correlation between the optical and X-ray breaks, but with a much shallower slope $\beta_3 = 0.39 \pm 0.27$, where the X-ray breaks increase moderately as the optical break frequency increases. Our analysis results show that the DRW model fits the ASAS-SN PSDs well. We also roughly recover the DRW break versus black hole mass relation measured in the literature. When high-frequency TESS PSDs are introduced, the DRW work less well. The broken power law fits show that the power law indices deviate from the DRW values of 0 and -2 as shown on the distributions on Figure 8, especially for the low-frequency slope. A few objects potentially have two break frequencies from the broken power law fits (Figure 7). This means that AGN variability is more complicated and may be governed by different physical processes at different scales. For example, the longer-term variability could be mainly described by a DRW model, physically related to MRI or other disk variability mechanisms, while the short-term optical variability is strongly affected by other disk variability mechanisms (e.g., Kelly et al. 2009; MacLeod et al. 2010).

- 1 H.Y. and X.D. would like to acknowledge NASA funds 80NSSC22K0488 and 80NSSC23K0379. Sup-
 2 port for T.J. was provided by NASA through the NASA Hubble Fellowship grant HF2-51509 awarded
 3 by the Space Telescope Science Institute, which is operated by the Association of Universities for
 4 Research in Astronomy, Inc., for NASA, under contract NAS5-26555.

REFERENCES

- Alard, C. 2000, *A&AS*, 144, 363
 Alard, C., & Lupton, R. H. 1998, *ApJ*, 503, 325
 Aranzana, E., K rding, E., Uttley, P., Scaringi, S., & Bloemen, S. 2018, *MNRAS*, 476, 2501
 Balbus, S. A., & Hawley, J. F. 1991, *ApJ*, 376, 214
 Burke, C. J., Shen, Y., Chen, Y.-C., et al. 2020, *ApJ*, 899, 136
 Burke, C. J., Shen, Y., Blaes, O., et al. 2021, *Science*, 373, 789
 Butler, N. R., & Bloom, J. S. 2011, *AJ*, 141, 93
 Cackett, E. M., Chiang, C.-Y., McHardy, I., et al. 2018, *ApJ*, 857, 53
 Dai, X., Kochanek, C. S., Chartas, G., et al. 2010, *ApJ*, 709, 278
 Dexter, J., & Agol, E. 2011, *ApJ*, 727, L24
 Edelson, R., Gelbord, J. M., Horne, K., et al. 2015, *ApJ*, 806, 129
 Fausnaugh, M. M., Valley, P. J., Kochanek, C. S., et al. 2021, *ApJ*, 908, 51
 Gonz lez-Mart n, O. 2018, *ApJ*, 858, 2
 Gonz lez-Mart n, O., & Vaughan, S. 2012, *A&A*, 544, A80
 Grandi, P., Tagliaferri, G., Giommi, P., Barr, P., & Palumbo, G. G. C. 1992, *ApJS*, 82, 93
 Haardt, F., & Maraschi, L. 1991, *ApJ*, 380, L51
 Henden, A. A., Levine, S., Terrell, D., & Welch, D. L. 2015, in *American Astronomical Society Meeting Abstracts*, Vol. 225, *American Astronomical Society Meeting Abstracts #225*, 336.16
 Jayasinghe, T., Kochanek, C. S., Stanek, K. Z., et al. 2018, *MNRAS*, 477, 3145
 Jayasinghe, T., Stanek, K. Z., Kochanek, C. S., et al. 2019, *MNRAS*, 485, 961
 Jha, V. K., Joshi, R., Chand, H., et al. 2022, *MNRAS*, 511, 3005
 Kasliwal, V. P., Vogeley, M. S., & Richards, G. T. 2015, *MNRAS*, 451, 4328
 Kaspi, S., Smith, P. S., Netzer, H., et al. 2000, *ApJ*, 533, 631

- Kawaguchi, T., Mineshige, S., Umemura, M., & Turner, E. L. 1998, *ApJ* , 504, 671
- Kelly, B. C., Bechtold, J., & Siemiginowska, A. 2009, *ApJ* , 698, 895
- Kochanek, C. S., Shappee, B. J., Stanek, K. Z., et al. 2017, *PASP* , 129, 104502
- Kozłowski, S. 2016, *ApJ* , 826, 118
- Lightman, A. P., & Eardley, D. M. 1974, *ApJ* , 187, L1
- Lomb, N. R. 1976, *Ap&SS* , 39, 447
- MacLeod, C. L., Ivezić, Ž., Kochanek, C. S., et al. 2010, *ApJ* , 721, 1014
- MacLeod, C. L., Brooks, K., Ivezić, Ž., et al. 2011, *ApJ* , 728, 26
- Markowitz, A., Edelson, R., & Vaughan, S. 2003, *ApJ* , 598, 935
- McHardy, I. M., Papadakis, I. E., Uttley, P., Page, M. J., & Mason, K. O. 2004, *MNRAS* , 348, 783
- McHardy, I. M., Connolly, S. D., Horne, K., et al. 2018, *MNRAS* , 480, 2881
- Morgan, C. W., Kochanek, C. S., Dai, X., Morgan, N. D., & Falco, E. E. 2008, *ApJ* , 689, 755
- Mushotzky, R. F., Done, C., & Pounds, K. A. 1993, *ARA&A* , 31, 717
- Mushotzky, R. F., Edelson, R., Baumgartner, W., & Gandhi, P. 2011, *ApJ* , 743, L12
- Peterson, B. M., Bentz, M. C., Desroches, L.-B., et al. 2005, *ApJ* , 632, 799
- Ptak, A., Yaqoob, T., Mushotzky, R., Serlemitsos, P., & Griffiths, R. 1998, *ApJ* , 501, L37
- Reynolds, C. S., & Miller, M. C. 2009, *ApJ* , 692, 869
- Ricker, G. R., Winn, J. N., Vanderspek, R., et al. 2015, *JATIS* , 1, 014003
- Ruan, J. J., Anderson, S. F., MacLeod, C. L., et al. 2012, *ApJ* , 760, 51
- Scargle, J. D. 1982, *ApJ* , 263, 835
- Shakura, N. I., & Sunyaev, R. A. 1976, *MNRAS* , 175, 613
- Shappee, B., Prieto, J., Stanek, K. Z., et al. 2014a, in *American Astronomical Society Meeting Abstracts, Vol. 223, American Astronomical Society Meeting Abstracts #223*, 236.03
- Shappee, B. J., Prieto, J. L., Grupe, D., et al. 2014b, *ApJ* , 788, 48
- Simm, T., Salvato, M., Saglia, R., et al. 2016, *A&A* , 585, A129
- Smith, K. L., Mushotzky, R. F., Boyd, P. T., et al. 2018, *ApJ* , 857, 141
- Treiber, H. P., Hinkle, J. T., Fausnaugh, M. M., et al. 2022, *arXiv e-prints*, arXiv:2209.15019
- Trèvese, D., & Vagnetti, F. 2002, *ApJ* , 564, 624
- Troyer, J., Starkey, D., Cackett, E. M., et al. 2016, *MNRAS* , 456, 4040
- Uttley, P., McHardy, I. M., & Papadakis, I. E. 2002, *MNRAS* , 332, 231
- Vallely, P. J., Kochanek, C. S., Stanek, K. Z., Fausnaugh, M., & Shappee, B. J. 2021, *MNRAS* , 500, 5639
- Vanden Berk, D. E., Wilhite, B. C., Kron, R. G., et al. 2004, *ApJ* , 601, 692
- Vanderspek, R., Doty, J. P., Fausnaugh, M., et al. 2018, *TESS Instrument Handbook*, Tech. rep., Kavli Institute for Astrophysics and Space Science, Massachusetts Institute of Technology
- Vaughan, S., Edelson, R., Warwick, R. S., & Uttley, P. 2003, *MNRAS* , 345, 1271
- Wandel, A., Peterson, B. M., & Malkan, M. A. 1999, *ApJ* , 526, 579
- Yuk, H., Dai, X., Jayasinghe, T., et al. 2022, *ApJ* , 930, 110